JM PAPERS

CrossMark

Force balance in rapidly rotating Rayleigh–Bénard convection

Andrés J. Aguirre Guzmán[1], **Matteo Madonia**[1], **Jonathan S. Cheng**[1],[‡],
Rodolfo Ostilla-Mónico[2], **Herman J.H. Clercx**[1] **and Rudie P.J. Kunnen**[1],[†]

[1]Fluids and Flows group, Department of Applied Physics and J. M. Burgers Centre for Fluid Dynamics, Eindhoven University of Technology, P.O. Box 513, 5600 MB Eindhoven, The Netherlands

[2]Department of Mechanical Engineering, University of Houston, Houston, TX 77004, USA

The force balance of rotating Rayleigh–Bénard convection regimes is investigated using direct numerical simulation on a laterally periodic domain, vertically bounded by no-slip walls. We provide a comprehensive view of the interplay between governing forces both in the bulk and near the walls. We observe, as in other prior studies, regimes of cells, convective Taylor columns, plumes, large-scale vortices (LSVs) and rotation-affected convection. Regimes of rapidly rotating convection are dominated by geostrophy, the balance between Coriolis and pressure-gradient forces. The higher-order interplay between inertial, viscous and buoyancy forces defines a subdominant balance that distinguishes the geostrophic states. It consists of viscous and buoyancy forces for cells and columns, inertial, viscous and buoyancy forces for plumes, and inertial forces for LSVs. In rotation-affected convection, inertial and pressure-gradient forces constitute the dominant balance; Coriolis, viscous and buoyancy forces form the subdominant balance. Near the walls, in geostrophic regimes, force magnitudes are larger than in the bulk; buoyancy contributes little to the subdominant balance of cells, columns and plumes. Increased force magnitudes denote increased ageostrophy near the walls. Nonetheless, the flow is geostrophic as the bulk. Inertia becomes increasingly more important compared with the bulk, and enters the subdominant balance of columns. As the bulk, the near-wall flow loses rotational constraint in rotation-affected convection. Consequently, kinetic boundary layers deviate from the expected behaviour from linear Ekman boundary layer theory. Our findings elucidate the dynamical balances of rotating thermal convection under realistic top/bottom boundary conditions, relevant to laboratory settings and large-scale natural flows.

Key words: rotating flows

† Email address for correspondence: r.p.j.kunnen@tue.nl
‡ Current address: Department of Mechanical Engineering, University of Rochester, Rochester, NY 14627, USA.

928 A16-1

1. Introduction

Buoyancy and rotational forces drive and shape many large-scale flows in nature, such as swirling convection currents of conductive material in the Earth's outer core that generate the Earth's magnetic field (Cardin & Olson 1994; Glatzmaier *et al.* 1999; Jones 2000; Sarson 2000; Aubert, Gastine & Fournier 2017; Schaeffer *et al.* 2017; Guervilly, Cardin & Schaeffer 2019), deep convection in the world's oceans (Marshall & Schott 1999; Gascard *et al.* 2002; Wadhams *et al.* 2002; Budéus *et al.* 2004) and trade winds near the Earth's surface in the atmosphere (Hadley 1735). The influence of these forces is also observed beyond our own planet: as deep convection in the interior of gaseous planets (Busse & Carrigan 1976; Busse 1994; Yadav & Bloxham 2020) and zonal flows in their atmosphere (Ingersoll 1990; Sanchez-Lavega, Rojas & Sada 2000; Porco *et al.* 2003; Heimpel & Aurnou 2007; Heimpel, Gastine & Wicht 2016; Cabanes *et al.* 2017), as well as in the convection zone of stars like our Sun (Miesch 2000; Cattaneo, Emonet & Weiss 2003; Balbus *et al.* 2009; Hindman, Featherstone & Julien 2020).

Understanding the dynamics of these geophysical and astrophysical flows is paramount, however, their sheer size, remoteness and complexity preclude their direct investigation. A relatively simple, but highly relevant framework to investigate these flows is provided by the problem of rotating Rayleigh–Bénard convection (RRBC), where a rotating fluid layer is heated from below and cooled from above. In this system, the Rayleigh number Ra parameterises the strength of the thermal forcing, the Ekman number Ek (and, alternatively, the convective Rossby number Ro_C) measures the strength of rotation, and the Prandtl number Pr involves the diffusive properties of the fluid. Large-scale flows are characterised by extreme values of these governing parameters. In the Earth's outer core, Ra is estimated to be $O(10^{20} - 10^{30})$, $Ek \sim O(10^{-15})$ and $Pr \sim O(10^{-2} - 10^{-1})$. Such conditions are certainly unfeasible for present-day simulations and experiments, yet studies at moderate parameter values have made great strides towards understanding the flow phenomenology in RRBC – see Kunnen (2021) for a recent review. In particular, it has been observed that a plethora of convection states exists in the range between rapidly rotating and non-rotating convection. Specifically, the parameter space of RRBC is partitioned into several regimes where the flow manifests as: quasi-steady convection cells (Chandrasekhar 1961); convective Taylor columns (only at $Pr \gtrsim 2$) (Sakai 1997; Sprague *et al.* 2006; Grooms *et al.* 2010; Kunnen, Clercx & Geurts 2010; Julien *et al.* 2012; King & Aurnou 2012; Rajaei, Kunnen & Clercx 2017; Noto *et al.* 2019; Chong *et al.* 2020; Shi *et al.* 2020), plumes (Sprague *et al.* 2006; Kunnen *et al.* 2010; Julien *et al.* 2012; Rajaei *et al.* 2017; Maffei *et al.* 2021); geostrophic turbulence (Sprague *et al.* 2006; Julien *et al.* 2012; Maffei *et al.* 2021; Rubio *et al.* 2014; Stellmach *et al.* 2014); rotation-affected convection (Ecke & Niemela 2014; Kunnen *et al.* 2016); and non-rotating convection (Malkus 1954; Kraichnan 1962; Spiegel 1971; Castaing *et al.* 1989; Ahlers, Grossmann & Lohse 2009; Lohse & Xia 2010). The cellular regime is typically found in the range $1 \lesssim Ra/Ra_c \lesssim 2$ ($Ra_c \sim Ek^{-4/3}$ is the critical Rayleigh number for onset of convection), and consists of narrow quasi-steady cells with horizontal size $\ell_c \sim Ek^{1/3}$ (Chandrasekhar 1961). Columns manifest at larger Ra/Ra_c, and are surrounded by 'shields' of opposite vertical vorticity and opposite temperature fluctuation. With increasing Ra/Ra_c, the shields become weaker and the vortical columns interact with each other. As a result, their vertical coherence is affected, leading to the development of plumes. At larger Ra/Ra_c, the geostrophic turbulence regime manifests. The combination of turbulence and strong rotational constraint leads to a quasi-two-dimensional dynamics that enables the transfer of kinetic energy from small to large spatial scales. This upscale energy transfer can lead to the formation of large-scale vortices (LSVs). In the rotation-affected regime, no

upscale energy transfer is present (Kunnen *et al.* 2016) as rotational forces are no longer dominant, instead the turbulent flow is thought to be dominated by buoyancy. Finally, in the non-rotating convection regime, Coriolis forces have no dynamical effect.

Numerous investigations into the interplay amongst the forces governing RRBC have been primarily focussed on the determination of the most relevant forces in geophysical and astrophysical settings. These studies aim to determine the dominant force balance in these large-scale flows in order to estimate the characteristic flow velocity and characteristic length scale of the convective motions therein (Stevenson 1979; Aubert *et al.* 2001; Christensen 2002; Aubert 2005; King & Buffett 2013; King, Stellmach & Buffett 2013; Aurnou *et al.* 2015; Gastine, Wicht & Aubert 2016; Guervilly *et al.* 2019; Aurnou, Horn & Julien 2020). However, the role of subdominant forces has not been addressed extensively. A complete view of the interplay between all forces is required to effectively characterise the flow and its transitional behaviours between regimes. In this study, we focus on fully understanding the force balance, from the leading contributors to the subdominant forces. Previous efforts have been made in this direction in the field of rotating magnetoconvection (Soderlund, King & Aurnou 2012; Calkins *et al.* 2015; Yadav *et al.* 2016; Aubert *et al.* 2017; Aubert 2019; Schwaiger, Gastine & Aubert 2021). Self-sustained convective dynamos in planetary systems operate in a rotationally constrained regime. There, a balance is thought to hold amongst the Coriolis, pressure gradient, buoyancy and Lorentz forces, also known as magneto–Archimedean–Coriolis (MAC) balance. Hence, many studies seek to determine the specific parameter values and length scales at which the contribution of viscous and inertial forces becomes negligible, and therefore a MAC balance is possible. In our simulations of non-magnetic, rotating convection in a horizontal plane fluid layer, we access both low-supercriticality flow regimes, where viscous effects are expected to be significant, and highly supercritical regimes, where we foresee an increased importance of inertial forces. Similar low- and high-supercriticality RRBC flows have been studied by means of asymptotically reduced equations (Sprague *et al.* 2006; Julien *et al.* 2012; Plumley *et al.* 2016; Maffei *et al.* 2021), valid at $Ek, Ro_C \rightarrow 0$. In these studies the geostrophic regimes (cells, columns, plumes and geostrophic turbulence with LSVs) are charted. Here, we assess the force balance of the full Navier–Stokes equations in these regimes and at larger Ra/Ra_c in the rotation-affected regime. We identify flow transitions as distinct changes in the dominant or subdominant force balance, leading to a natural identification of each regime. We mainly consider the case of no-slip walls. This type of boundary condition is especially relevant to realistic settings such as laboratory experiments and large-scale flows in nature.

The remainder of this paper is structured as follows. Section 2 introduces the equations of motion of RRBC, as well as the equations used to calculate the force magnitudes. In § 3, we describe the numerical method and tabulate the parameter values for the simulations. In § 4.1 we present the flow structures observed for the explored parameter values. The midheight magnitude of the forces is discussed in § 4.2 as a function of the flow supercriticality. There, we also identify the characteristic force balance of the distinct flow regimes. The interplay amongst the forces in the region close to the no-slip walls is investigated in § 4.3. Finally, in § 5 we present our conclusions.

2. Governing equations and dimensionless parameters

We consider the buoyancy-driven flow between two parallel horizontal walls, with relative temperature difference $\Delta T = T_{bottom} - T_{top} > 0$, separated by a vertical distance H. The rotation vector $\Omega \hat{z}$ is parallel to the vertical unit vector $\hat{z}$, whereas the gravitational acceleration is $\boldsymbol{g} = -g\hat{z}$. The flow is incompressible, and the kinematic viscosity, thermal

diffusivity and thermal expansion coefficient of the fluid are ν, κ and α, respectively. We model rotating thermal convection by using the non-dimensional Navier–Stokes and heat equations in the Boussinesq approximation (Chandrasekhar 1961),

$$\frac{\partial \boldsymbol{u}}{\partial t} = -(\boldsymbol{u} \cdot \boldsymbol{\nabla})\boldsymbol{u} - \frac{1}{Ro_C}\hat{z} \times \boldsymbol{u} - \boldsymbol{\nabla}p + \sqrt{\frac{Pr}{Ra}}\nabla^2\boldsymbol{u} + \theta\hat{z}, \tag{2.1}$$

$$\frac{\partial \theta}{\partial t} + (\boldsymbol{u} \cdot \boldsymbol{\nabla})\theta = \frac{1}{\sqrt{RaPr}}\nabla^2\theta, \tag{2.2}$$

with the incompressibility constraint

$$\boldsymbol{\nabla} \cdot \boldsymbol{u} = 0. \tag{2.3}$$

We use H, ΔT and the characteristic 'free-fall' velocity scale $U_{ff} = \sqrt{g\alpha\Delta TH}$ to obtain the non-dimensional velocity $\boldsymbol{u}$, temperature θ, pressure p and time t. Equations (2.1) and (2.2) involve three non-dimensional parameters,

$$Ra = \frac{g\alpha\Delta TH^3}{\nu\kappa}, \quad Pr = \frac{\nu}{\kappa}, \quad Ro_C = \frac{\sqrt{g\alpha\Delta T/H}}{2\Omega}, \tag{2.4a–c}$$

where Ra is the Rayleigh number, Pr is the Prandtl number and the convective Rossby number Ro_C parameterises the (inverse) strength of rotation. Alternatively, the strength of rotation can be quantified by means of the Ekman number $Ek = \nu/(2\Omega H^2)$, which provides the ratio of viscous to Coriolis forces. A convenient relation between the various dimensionless parameters is $Ro_C = Ek(Ra/Pr)^{1/2}$.

The velocity field in (2.1)–(2.3) must fulfil the impenetrable no-slip boundary condition $\boldsymbol{u} = \boldsymbol{0}$ at the walls. Cases with stress-free boundary conditions comply with $\partial u/\partial z = \partial v/\partial z = 0$ and $w = 0$ at the walls. The temperature field must meet the conducting boundary condition $\theta = 1$ at the bottom and $\theta = 0$ at the top.

Rotation, contrary to convection, has a stabilising effect on the flow. Therefore, at low values of the Rayleigh number and sufficiently strong rotation (low Ek and Ro_C), no convective motions take place, and the heat transfer from bottom to top boundary is exclusively due to conduction. In a laterally unbounded fluid layer subject to rapid rotation ($Ek \lesssim 10^{-3}$), the critical Rayleigh number Ra_c for the onset of convection is given by

$$Ra_c = \begin{cases} 17.4(Ek/Pr)^{-4/3} & \text{for } Pr < 0.68, \\ 8.7Ek^{-4/3} & \text{for } Pr \geq 0.68 \end{cases} \tag{2.5}$$

(Chandrasekhar 1961; Aurnou *et al.* 2018). Past this threshold, bulk convection starts in the form of oscillatory structures for $Pr < 0.68$, or steady cells for $Pr \geq 0.68$. Based on this critical value we define supercriticality as Ra/Ra_c, where Ra_c takes either definition in (2.5) depending on the Prandtl number of a given study case. Our results are presented as a function of Ra/Ra_c throughout this work.

The characteristic horizontal length scale ℓ_c (normalised by the domain height H) of the onset structures is given by

$$\ell_c = \begin{cases} 2.4(Ek/Pr)^{1/3} & \text{for } Pr < 0.68, \\ 2.4Ek^{1/3} & \text{for } Pr \geq 0.68 \end{cases} \tag{2.6}$$

(Chandrasekhar 1961; Heard & Veronis 1971; Julien *et al.* 2016), again, valid for a laterally unbounded layer of fluid and rapid rotation ($Ek \lesssim 10^{-3}$).

From (2.1), the governing forces of RRBC (the inertial, Coriolis, pressure gradient, viscous and buoyancy forces) are, in dimensionless form,

$$
\left.
\begin{aligned}
\boldsymbol{F}_I = -(\boldsymbol{u} \cdot \nabla)\boldsymbol{u}, \quad \boldsymbol{F}_C = -\frac{1}{Ro_C}\hat{\boldsymbol{z}} \times \boldsymbol{u}, \quad \boldsymbol{F}_P = -\nabla p, \\
\boldsymbol{F}_V = \sqrt{\frac{Pr}{Ra}}\nabla^2\boldsymbol{u}, \quad \boldsymbol{F}_B = \theta\hat{\boldsymbol{z}},
\end{aligned}
\right\}
\tag{2.7}
$$

respectively. Thus, the geostrophic balance can be written as $\boldsymbol{F}_C = -\boldsymbol{F}_P$. To estimate the magnitude of these forces, we follow a procedure inspired by that used by Aubert *et al.* (2017), Yadav *et al.* (2016), Aubert (2019), Schwaiger, Gastine & Aubert (2019) and Maffei *et al.* (2021). We compute the plane-averaged root mean square (r.m.s.) of each force. That is, for a given force $\boldsymbol{F}(\boldsymbol{x})$ with x-, y- and z-components $F_x(\boldsymbol{x})$, $F_y(\boldsymbol{x})$ and $F_z(\boldsymbol{x})$, its r.m.s. value is here defined as

$$
F(z) = \sqrt{\langle (F_x - \langle F_x \rangle)^2 + (F_y - \langle F_y \rangle)^2 + (F_z - \langle F_z \rangle)^2 \rangle},
\tag{2.8}
$$

where $\langle \cdot \rangle$ denotes averaging along the horizontal directions; therefore, F is a function of the vertical coordinate z only. In practice, on our laterally periodic domain, $\langle F_x \rangle \approx \langle F_y \rangle \approx \langle F_z \rangle \approx 0$ for the corresponding components of the inertial, Coriolis and viscous forces. For the pressure-gradient force and the buoyancy force, the deviations from the mean force components, e.g. $F_x - \langle F_x \rangle$, are considered in order to disregard the underlying mean vertical profiles of pressure and temperature; these profiles describe the mean hydrostatic balance in the system. Therefore, (2.8) enables the faithful calculation of the magnitude $|\boldsymbol{F}(\boldsymbol{x})|$ of the governing forces contributing to the dynamics in RRBC. We note that the plane-averaging procedure considers that the flow is statistically homogeneous in the horizontal directions. Hence, we are able to evaluate the spatial dependence of the force balance solely in terms of the vertical coordinate. The force components are calculated at each grid position on a horizontal cross-section. We consider a one single-time volume snapshot well within the statistically stationary state; for other snapshots within this state the results agree within 5 % on average.

3. Numerical set-up

Equations (2.1)–(2.3) are solved using direct numerical simulation on a horizontally periodic Cartesian domain. The simulations are performed using two codes, both based on the principal set-up of the Verzicco code (Verzicco & Orlandi 1996; Ostilla-Mónico *et al.* 2015). The codes differ in their approach to resolve the temperature field: one resolves both velocity and temperature on a single grid, and the other resolves temperature on a different grid than that for velocity. This distinction is due to the diffusive properties of the fluid, parameterised by the Prandtl number. Recall that the smallest active length scales for velocity and temperature fluctuations, i.e. the Kolmogorov length scale η_K and the Batchelor length scale η_B, respectively, are related by $\eta_B = \eta_K Pr^{-1/2}$. Hence, $\eta_K < \eta_B$ for fluids with low Prandtl number $Pr < 1$, whereas η_B is smaller for high $Pr > 1$. The latter property is exploited by the multiple-grid code in that it uses a finer grid to resolve the smaller temperature features, and a coarser grid to resolve the three-component velocity field. We use the single-grid code to simulate low-Pr fluid flows, and the multiple-grid code for cases at high Pr. A complete list of the cases investigated can be found in table 1.

The single-grid code is a Cartesian adaptation of the original Verzicco cylinder convection code (Verzicco & Orlandi 1996; Verzicco & Camussi 2003), where the

Pr	Ek	Ra	Ro_C	Ra/Ra_c	Nu	Γ	N_x	N_z	m_x	m_z	Flow
0.1	2.00×10^{-7}	1.00×10^{10}	0.063	14.48	7.21	0.302	1024	1408	—	—	LSV
0.1	2.24×10^{-7}	1.00×10^{10}	0.071	16.84	9.24	0.314	1024	1408	—	—	LSV
0.1	2.50×10^{-7}	1.00×10^{10}	0.079	19.50	11.14	0.326	768	1280	—	—	LSV*
0.1	3.00×10^{-7}	1.00×10^{10}	0.095	24.87	15.08	0.346	768	1280	—	—	LSV
0.1	4.00×10^{-7}	1.00×10^{10}	0.126	36.49	24.27	0.381	640	1280	—	—	LSV
0.1	8.00×10^{-7}	1.00×10^{10}	0.253	91.95	53.62	0.480	640	1280	—	—	RA
0.1	1.05×10^{-6}	1.00×10^{10}	0.332	132.14	66.15	0.526	768	1280	—	—	RA
0.1	2.80×10^{-6}	1.00×10^{10}	0.885	488.65	90.94	0.729	1088	1280	—	—	RA
0.1	6.00×10^{-6}	1.00×10^{10}	1.897	1349.95	98.70	0.940	1408	1280	—	—	RA
5.5	3.00×10^{-7}	5.50×10^{9}	0.009	1.27	2.46	0.323	256	640	2	1	C
5.5	3.00×10^{-7}	8.00×10^{10}	0.011	1.85	8.54	0.323	256	640	2	1	C
5.5	3.00×10^{-7}	1.00×10^{10}	0.013	2.31	18.59	0.323	384	640	2	1	T
5.5	3.00×10^{-7}	1.50×10^{10}	0.016	3.46	51.15	0.323	384	640	2	1	T
5.5	3.00×10^{-7}	2.00×10^{10}	0.018	4.62	64.78	0.323	384	640	2	1	T
5.2	1.00×10^{-7}	1.40×10^{11}	0.016	7.47	101.82	0.224	384	640	2	2	P*
5.2	1.00×10^{-7}	2.10×10^{11}	0.020	11.20	120.92	0.224	384	640	2	2	P
5.2	1.00×10^{-7}	3.20×10^{11}	0.025	17.07	137.84	0.224	512	640	2	2	P*
5.2	1.00×10^{-7}	6.00×10^{11}	0.034	32.01	187.27	0.224	512	640	2	2	P†
5.2	1.00×10^{-7}	9.50×10^{11}	0.043	50.68	247.73	0.224	640	896	2	2	LSV
5.2	1.00×10^{-7}	1.50×10^{12}	0.054	80.03	332.87	0.224	768	1024	2	2	LSV
100	3.00×10^{-7}	1.30×10^{11}	0.011	30.01	339.56	0.323	384	512	3	3	P
100	3.00×10^{-7}	2.10×10^{11}	0.014	48.48	401.93	0.323	384	512	3	3	P
100	3.00×10^{-7}	3.40×10^{11}	0.017	78.49	443.34	0.323	512	512	3	3	P
100	3.00×10^{-7}	6.00×10^{11}	0.023	138.50	505.35	0.323	512	768	3	3	P
100	3.00×10^{-7}	9.50×10^{11}	0.029	219.30	526.47	0.323	512	768	3	3	P
100	3.00×10^{-7}	1.50×10^{12}	0.037	346.26	622.14	0.323	512	768	3	3	P
100	3.00×10^{-7}	2.50×10^{12}	0.047	577.10	706.41	0.323	384	768	4	4	P

Table 1. Parameters for the simulations: Prandtl number Pr; Ekman number Ek; Rayleigh number Ra; convective Rossby number Ro_C; supercriticality Ra/Ra_c; and domain aspect ratio Γ. The slight difference in Pr between the $Pr \approx 5$ simulation series is for comparison with (ongoing) experiments in our group (Cheng *et al.* 2018, 2020). The Nusselt number Nu is the mean of five ways of measuring the convective heat transfer (discussed in the text). These measurements converge within 5 % of the mean value Nu. The number of grid points to resolve the velocity field are N_x and N_z ($N_y = N_x$), and the refinement factors for temperature m_x and m_z ($m_y = m_x$). The last column indicates the observed flow morphology: convective cells (C); convective Taylor columns (T); plumes (P); LSVs; or rotation-affected convection (RA). All cases are simulated with no-slip walls. Some cases, denoted with the superscript '*', are also independently simulated with stress-free boundaries. In the case denoted with '†' there are signs of upscale energy transfer, but no LSVs develop.

governing equations are discretised by second-order finite-differences with dynamic time stepping for the time advancement. The multiple-grid code, which also used this numerical scheme (Ostilla-Mónico *et al.* 2015), allows refinement of the grid for temperature in the x-, y- and z-directions independently, through the refinement factors m_x, m_y and m_z. In our domains the lateral sides are of equal length, thus $m_y = m_x$. The refinement is relative to the grid for velocity, thus m_x, m_y and m_z are selected based on the ratio $\eta_K/\eta_B = Pr^{1/2}$, and making sure to allocate an appropriate number of grid points within the thermal boundary layers (discussed below).

For all simulations the domain aspect ratio $\Gamma = W/H$ allows a sufficiently large sampling of convective structures, whose characteristic length scale ℓ_c is given by (2.6).

This procedure ensures the convergence of spatially averaged statistics. At low Pr, the domain size is $10\ell_c \times 10\ell_c \times 1$ (normalised by the domain height H). The multiple-grid strategy allows us to simulate high-Pr fluid flows much more efficiently compared with the single-grid code, thus facilitating the exploration of wider domains of size $20\ell_c \times 20\ell_c \times 1$ at high Pr.

Both codes use a grid with uniform horizontal spacing and non-uniform vertical distribution. In this way, a larger density of grid points can be placed near the walls to resolve the thin boundary layers. We verify, *a posteriori*, that a minimum of 11 grid points is allocated within the thinner (kinetic or thermal) boundary layer, which is enough to appropriately resolve it.

To validate the bulk resolution, we compare the grid spacing with the Kolmogorov and Batchelor length scales, η_K and η_B. We find that for low-Pr runs the bulk resolution is $\Delta z_u/\eta_K < 3$ and $\Delta z_\theta/\eta_B < 1$, where Δz_u and Δz_θ are the vertical grid spacing for the velocity and temperature field, respectively. For simulations at high Pr, we find $\Delta z_u/\eta_K < 3$ and $\Delta z_\theta/\eta_B < 3.7$. For all cases the horizontal grid spacing is smaller than the vertical one.

To further confirm the adequacy of the grid, we compute the time-averaged convective heat transfer Nu in five different ways: as the plane-averaged wall-normal temperature gradient at the bottom and at the top wall; as the volume-averaged convective flux; and the last two are based on exact relations for the dissipation rate of kinetic energy and thermal variance (Shraiman & Siggia 1990). For all cases the maximum difference between a given Nu and the mean of all Nu converges to better than a few per cent. This convergence is achieved over simulation times of the order of 10^2 convective time units. The mean Nu for all simulation cases is reported in table 1.

4. Results

4.1. *Flow structures*

Our RRBC survey spans a wide range of parameter values that jointly resolve over three decades of supercriticality Ra/Ra_c. This allows the exploration of distinct flow regimes: C, T, P, LSVs and RA. In our set of simulations at $Pr \approx 5$, we observe the regimes of cells, convective Taylor columns, plumes and large-scale vortices. We present visualisations of the temperature fluctuations in these regimes in figures 1(*a*) to 1(*d*), respectively. The large-scale vortices in figure 1(*d*) are better visualised in terms of the horizontal kinetic energy of the flow, as we show in figure 2(*a*). All of our simulation cases at $Pr = 100$ lie within the plumes regime; we show two example cases in figures 1(*e*) and 1(*f*). For the exploration of highly supercritical regimes we make use of a lower Prandtl number, $Pr = 0.1$. The reason is that sufficiently small values of Pr (i.e. smaller than 0.68, see (2.5)) act to decrease the critical Rayleigh number for onset of convection Ra_c. Thus, for a given value of Ra and Ek, low-Pr fluid flows can achieve a larger degree of supercriticality than those at high Pr. In other words, inertial effects are amplified in low-Pr fluids (Julien *et al.* 2012; Aurnou *et al.* 2018). At $Pr = 0.1$ we also observe large-scale vortices and, at larger Ra/Ra_c, we identify rotation-affected convection – see figures 1(*g*) and 1(*h*), respectively. Just like at $Pr \approx 5$, the LSVs are more clearly visualised in terms of the horizontal kinetic energy of the flow – we show this in figure 2(*b*). In the rotation-affected regime, convection becomes more three-dimensional and, in the particular case displayed in figure 1(*h*), the large parcel of hot fluid (red patch at the top) and large parcel of cold fluid (blue patch) resemble a large overturning cell similar to that observed in non-rotating convection. However, in this case, the magnitude of the Coriolis force is still appreciable
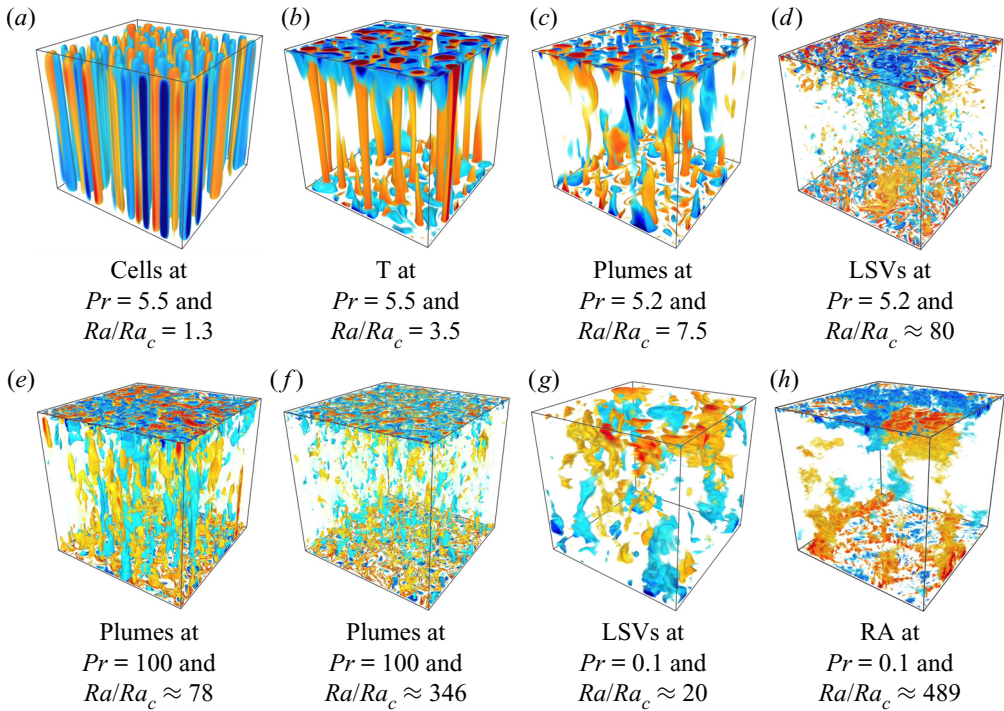
Figure 1. Temperature fluctuations for selected cases in the observed flow regimes. In the captions, T stands for convective Taylor columns, LSVs for large-scale vortices, RA for rotation-affected convection, Pr is Prandtl number and Ra/Ra_c is flow supercriticality. Owing to the low $Ek \sim 10^{-7}$ considered for all cases, the domain aspect ratio $\Gamma = W/H = O(Ek^{1/3})$ (W and H are its width and height) is smaller than unity, i.e. the computational domains are narrower than they are tall. Thus, for clarity, the domains are stretched horizontally by a factor $1/\Gamma$. The colour scale is chosen to highlight the flow features. Red denotes above-average temperature and blue is for below-average temperature.

as we shall discuss in §4.2. Finally, in order to discuss the observed flow regimes with increasing supercriticality, we present our results starting from simulations at $Pr \approx 5$ and 100, and then at $Pr = 0.1$.

4.2. *Force balance in the bulk*

In figure 3(a,c,e) we plot the magnitudes of the governing forces as a function of Ra/Ra_c. The plots correspond to our results from simulations at Prandtl numbers $Pr \approx 5$, 100 and 0.1, respectively. The forces are calculated at half the domain height; we find that these results are representative of the bulk dynamics. Figure 3(a) shows the forces at $Pr \approx 5$, where we observe cells, convective Taylor columns, plumes and large-scale vortices. The figure shows that in these regimes not only are the Coriolis and pressure-gradient forces larger than the other forces in the flow, but they are also in close balance with each other. Thus, the flows are indeed in geostrophic balance at leading order. This is also observed for plumes at $Pr = 100$, in figure 3(c), and LSVs at $Pr = 0.1$, in figure 3(e). The simulation cases with stress-free boundary conditions at $Pr \approx 5$ and 0.1 are also directed by the geostrophic balance, as seen in figures 3(a) and 3(e), respectively. The presence of a leading-order geostrophic balance in rotationally constrained convection is exploited in quasi-geostrophic models (Charney 1948; Busse 1970; Charney 1971; Cardin & Olson
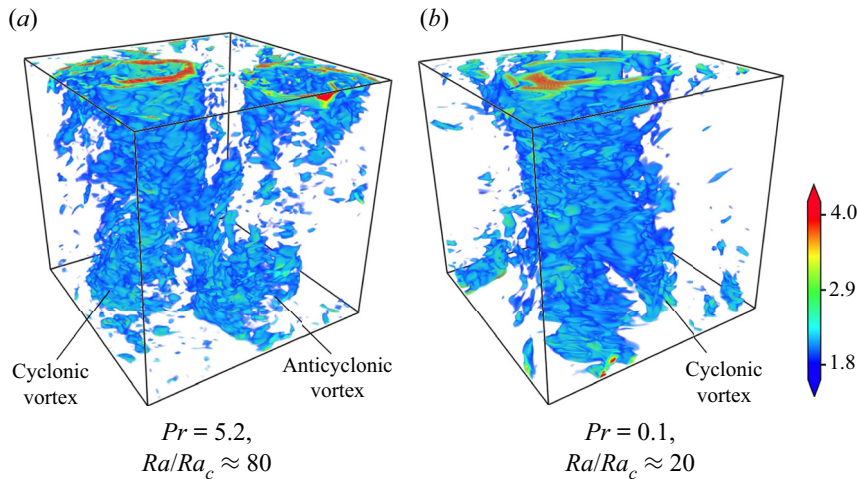
Figure 2. Horizontal kinetic energy, scaled by volume-averaged total energy, for LSV cases in figures 1(*d*) and 1(*g*). As before, the domains are stretched horizontally by a factor $1/\Gamma$ for clarity. Both plots have the same colour scale.

1994; Julien, Knobloch & Werne 1998; Aubert, Gillet & Cardin 2003; Gillet & Jones 2006; Julien *et al.* 2006; Sprague *et al.* 2006; Calkins *et al.* 2012; Julien *et al.* 2012; Rubio *et al.* 2014; Julien *et al.* 2016) to simplify the governing equations in the limit of rapid rotation.

To further illustrate the dominant role of rotation, we directly compute the local Rossby number Ro_ℓ as the ratio of the local estimates of inertial to Coriolis forces: $Ro_\ell = F_I/F_C$. Notice that this Rossby number is different from the convective Rossby number Ro_C in (2.4*a–c*). In figure 3(*b,d,f*) we plot both local and convective Rossby numbers. Let us first discuss Ro_ℓ, shown as black squares in the aforementioned figures. Figure 3(*b*) shows that $Ro_\ell < 1$ for all the geostrophic regimes (i.e. cellular, columnar, plumes and LSVs regimes), which is a clear sign of rotational constraint. Figures 3(*d*) and 3(*f*) reveal the same for plumes at $Pr = 100$ and LSVs at $Pr = 0.1$, respectively. Nevertheless, in figure 3(*f*) for $Pr = 0.1$ cases, we see that Ro_ℓ becomes larger than 1 for values of supercriticality larger than 60. This is due to the decrease in strength of the Coriolis force and the increase in inertial force at $Ra/Ra_c > 60$, as evidenced in figure 3(*e*). This indicates that the flow transitions to a state where rotation affects the flow, but no longer dominates it. In this so-called regime of rotation-affected convection, geostrophy does not constitute the primary force balance in the flow. Instead, pressure gradient and inertial forces are dominant. The green symbols in figure 3(*e*) represent the quantity $|\boldsymbol{F}_C + \boldsymbol{F}_P|$, which is only comparable to F_P in this regime because F_C is much smaller; we shall discuss this quantity below. In figure 3(*b*), the local Rossby number Ro_ℓ for cells and columns is fitted by the predicted scaling Ra^2 for rotationally constrained convection in King *et al.* (2013) with a r.m.s. error of 3.7 %. This scaling is suggested for $RaEk^{3/2} < 10$, or $Ra/Ra_c \lesssim 14$ at $Ek = 3 \times 10^{-7}$, as in our simulations (see table 1). Moreover, the predicted scaling is for a flow in visco–Archimedean–Coriolis (VAC) balance, i.e. the triple balance between viscous, buoyancy and rotational forces. Below we confirm that these regimes do exhibit this force balance, and show that it is subdominant in our simulations (see table 2). Also in figure 3(*b*), a least-squares fit of the Ro_ℓ values for plumes at $Pr \approx 5$ yields a scaling $(Ra/Ra_c)^{0.8}$. This scaling fits the Ro_ℓ data of plumes at $Pr = 100$, too, with an r.m.s. error of approximately 10 %. Overall, Ro_ℓ proves to be a good
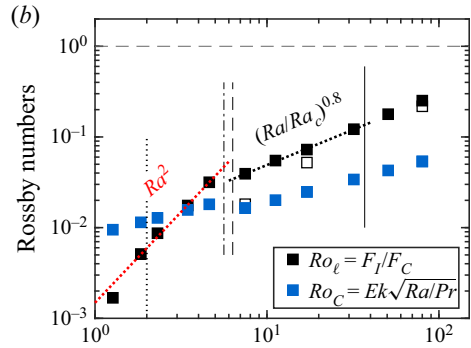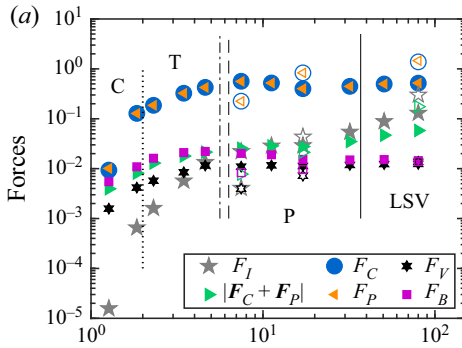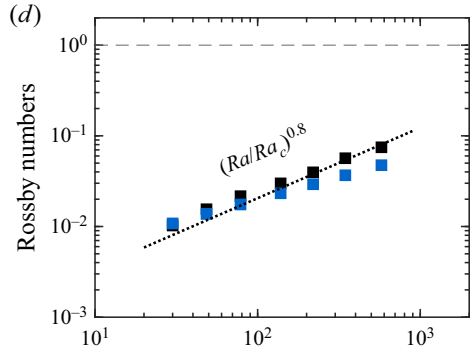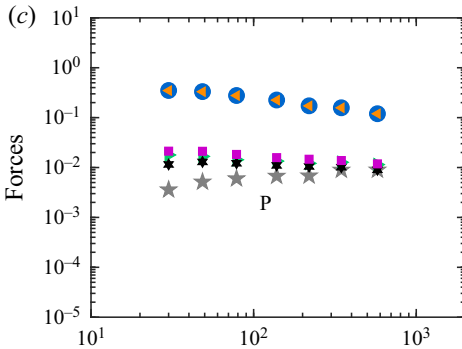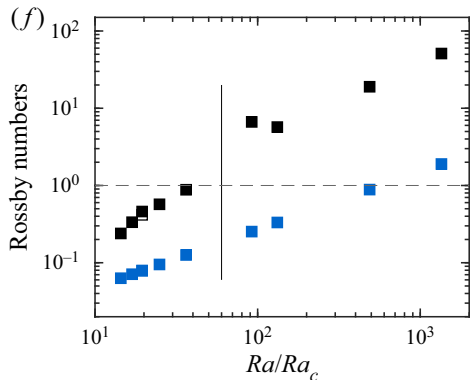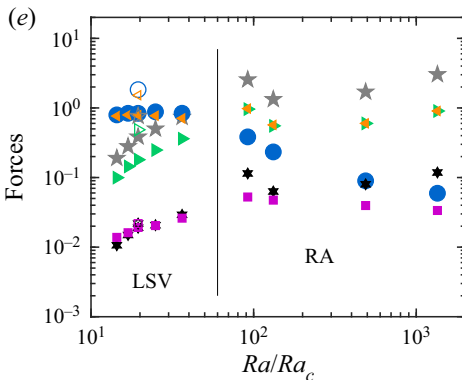
Figure 3. Force balance (*a*,*c*,*e*) and local Rossby number Ro_ℓ (*b*,*d*,*f*), both at midheight, as a function of supercriticality Ra/Ra_c for simulations at (*a*,*b*) $Pr \approx 5$, (*c*,*d*) 100 and (*e*,*f*) 0.1. The convective Rossby number $Ro_C = Ek\sqrt{Ra/Pr}$ is plotted along with Ro_ℓ for comparison. Filled and open symbols correspond to simulations with no-slip and stress-free boundary conditions, respectively. Vertical dotted lines denote our estimated transition between C and T. Vertical dash–dotted and dashed lines are the predicted transitions between T and P in Cheng *et al.* (2015) and Nieves, Rubio & Julien (2014), respectively. Vertical solid lines are our estimated transitions between plumes and large-scale vortices (LSVs, at $Pr \approx 5$), and between LSVs and RA convection (at $Pr = 0.1$). Horizontal dashed lines indicate $Ro_\ell, Ro_C = 1$, the red dotted line is the predicted scaling in King *et al.* (2013), and the (thick) black dotted lines result from the least-squares fit of cases with plumes at $Pr \approx 5$.

Flow	Dominant force balance	Subdominant force balance
Cells	$F_C \sim F_P$	$F_{ageos} \sim F_V \sim F_B$
Columns	$F_C \sim F_P$	$F_{ageos} \sim F_V \sim F_B$
Plumes	$F_C \sim F_P$	$F_{ageos} \sim F_I \sim F_V \sim F_B$
LSVs	$F_C \sim F_P$	$F_{ageos} \sim F_I$
RA convection	$F_I \sim F_P$	$F_C \sim F_V \sim F_B$

Table 2. Dominant and subdominant force balances at midheight ($z = 0.5$) for each flow regime. Here, $F_{ageos} = |\boldsymbol{F}_{ageos}| \equiv |\boldsymbol{F}_C + \boldsymbol{F}_P|$ measures the ageostrophy of the flow, i.e. the deviation from geostrophic balance caused by the presence of the remaining forces.

indicator of the underlying dynamical balance of the distinct flow regimes. Conversely, the convective Rossby number Ro_C fails to provide such diagnosis; though both Rossby numbers are comparable for our $Pr = 100$ cases (figure 3d). Interestingly, in figure 3(b), the crossing of Ro_ℓ and Ro_C (at $Ra/Ra_c \approx 3$) illustrates the effect of turbulence: upon decreasing Ra/Ra_c, the flow is no longer turbulent and Ro_ℓ steeply decreases as inertial forces plummet.

The leading-order balance between Coriolis and pressure-gradient forces in the regimes of cells, columns, plumes and LSVs constrains the flow to two dimensions, in accordance with the Taylor–Proudman theorem (Proudman 1916; Taylor 1917). However, the participation of other forces (buoyancy, viscous and inertial) in the force balance (see figure 3a,c,e) leads to deviations from geostrophy, denoted by the difference between Coriolis and pressure-gradient forces $\boldsymbol{F}_C + \boldsymbol{F}_P$. As a result, these geostrophic flows are actually ageostrophic at higher order. Figure 3(a) shows that for cells and columns, at $Ra/Ra_c < 6$, $|\boldsymbol{F}_C + \boldsymbol{F}_P|$ mostly originates from buoyancy with some contribution of the viscous force, whereas the magnitude of the inertial force remains relatively small. These observations concur with results from asymptotic studies in Julien *et al.* (2012). The absence of inertial forces, and thus the presence of a VAC balance in rotationally constrained convection is leveraged in single-mode theories by Grooms *et al.* (2010) and Portegies *et al.* (2008) to provide an analytical model for the convective Taylor columns. Nonetheless, inertia does increase rapidly with Ra/Ra_c. In fact, at $Ra/Ra_c \gtrsim 6$, inertia becomes part of the subdominant force balance. The participation of inertial forces in this subdominant balance affects the vertical coherence of the flow, which results in its transition from vertically aligned columns to plumes with weaker vertical coherence. For the $Pr = 100$ cases shown in figure 3(a), the magnitude of the inertial force is smaller due the larger kinematic viscosity of the fluid (relative to its thermal diffusivity). However, inertia becomes increasingly important with Ra/Ra_c, leading to plumes with an ever greater degree of vertical incoherence, as displayed in figure 1(e,f). In the LSV regime at $Pr \approx 5$ and $Ra/Ra_c \gtrsim 37$, inertia becomes larger than $|\boldsymbol{F}_C + \boldsymbol{F}_P|$, although it does remain smaller than F_C and F_P. This is also observed at $Pr = 0.1$, see figure 3(e). Whilst inertial forces are the main source of ageostrophy for plumes and LSVs, buoyancy also participates in the force balance. This is more clearly evidenced in figure 4, where the force balance of cases at $Pr \approx 5$ is decomposed into its horizontal and vertical components (similar results are obtained at $Pr = 0.1$ and 100; a combination of the horizontal and vertical components according to (2.8) results in the full force balance displayed in figure 3a). In figure 4(a), as expected, the geostrophic balance in all cases is seen to dominate the horizontal force balance, whereas the balance between the inertial force and $|\boldsymbol{F}_C + \boldsymbol{F}_P|$ indicates that inertia is the primary cause of
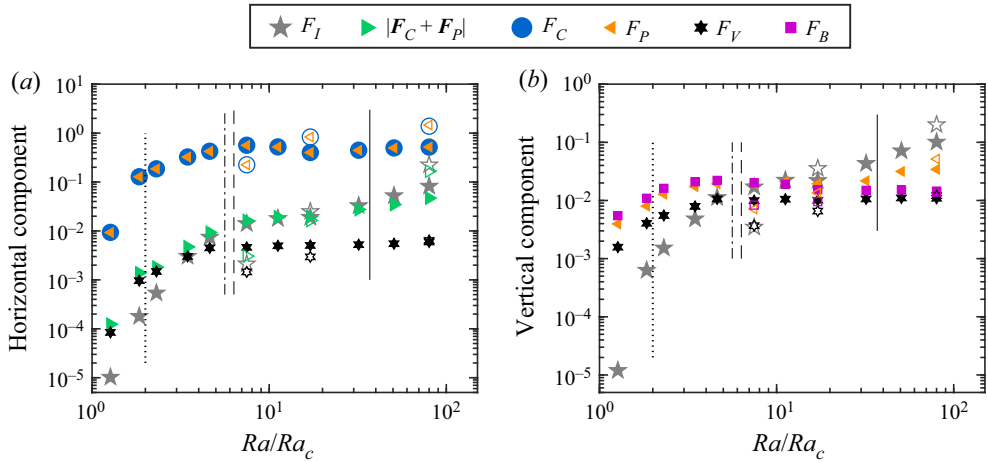
Figure 4. (*a*) Horizontal and (*b*) vertical force balance at midheight as a function of the flow supercriticality Ra/Ra_c, for simulations at $Pr \approx 5$. Vertical lines are as in figure 3.

ageostrophy in the plumes and LSV regimes. On the other hand, figure 4(*b*) reveals that for all cases there is an approximate balance between the buoyancy force and vertical pressure-gradient force. The presence of this so-called hydrostatic balance highlights the importance of buoyancy. It is therefore reasonable to assume that the dynamics of plumes and LSVs results from the balance between the Coriolis, inertial and buoyancy forces, also known as the Coriolis–inertia–Archimedean (CIA) balance, with some contribution of the viscous force in the plumes regime. These observations are consistent with results from asymptotic simulations (Julien *et al.* 2012). In figure 3(*e*), we see that at $Ra/Ra_c \gtrsim 60$, the inertial force is part of the dominant force balance, and the flow transitions to the rotation-affected regime. Finally, from figures 3(*a*) and 3(*b*), we can estimate an upper limit for the LSV regime or, equivalently, the transition to RA convection, as the Ra/Ra_c value at which the inertial force becomes part of the dominant force balance or, similarly, the value at which Ro_ℓ becomes larger than one. We estimate that this occurs at $Ra/Ra_c \approx 400$. In table 2 we present a summary of the dominant and subdominant force balances in all flow states.

To further illustrate how changes in the force balance affect the flow, we analyse the midheight r.m.s. values of the horizontal velocity u_{RMS} and vertical velocity w_{RMS} as a function of Ra/Ra_c. Following the definitions in Kunnen, Geurts & Clercx (2009) and Kerr (1996): $u_{RMS} = \sqrt{\langle u^2 \rangle + \langle v^2 \rangle}$ and $w_{RMS} = \sqrt{\langle w^2 \rangle}$, where $\langle \cdot \rangle$ denotes time- and plane-averaging. At all heights, we have verified that $\langle u \rangle \approx \langle v \rangle \approx 0$, so that no mean horizontal flows are established across the periodic domain and that $\langle w \rangle \approx 0$ owing to the incompressibility constraint. Figure 5 shows that for cells and columns, at $Ra/Ra_c \lesssim 6$, the participation of buoyancy in the subdominant force balance yields large vertical velocity fluctuations. Conversely, the smaller contribution of inertial forces may be associated with low variability of horizontal velocities, strengthening the Taylor–Proudman constraint and so the vertical alignment of the flow structures in this regime. In the plumes regime, where inertial forces are as important as buoyancy, we see that the magnitude of horizontal velocity fluctuations is comparable to that of vertical fluctuations. Throughout the LSV regime at both $Pr \approx 5$ and 0.1, where the magnitude of inertial forces is even larger, horizontal velocity fluctuations are larger. This may result in a nearly two-dimensional turbulent state, where energy can be transferred from small to large scales, leading to
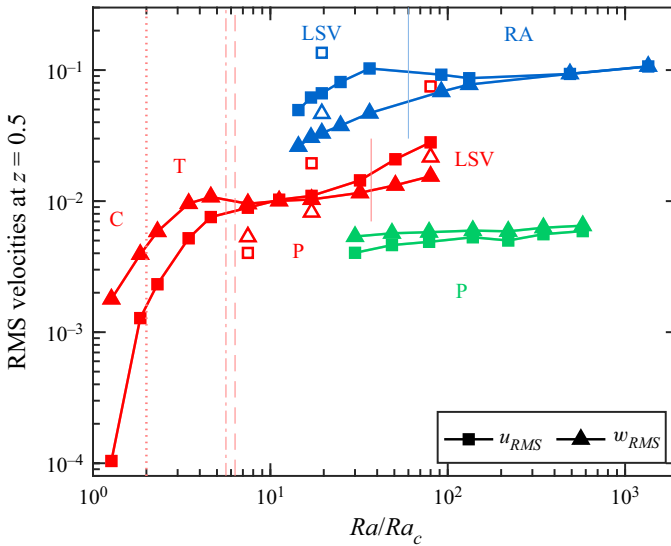
928 A16-12

Figure 5. Root mean square of horizontal and vertical velocities, u_{RMS} and w_{RMS}, respectively, at midheight $z = 0.5$. Filled and open symbols correspond to simulations with no-slip and stress-free boundary conditions, respectively. Red, green and blue symbols are results from simulations at $Pr \approx 5$, 100 and 0.1, respectively. Colour-coded vertical lines and regime labels are as in figure 3.

the formation of LSVs (the dynamics of LSVs in presence of no-slip walls is discussed in Aguirre Guzmán *et al.* (2020)). Finally, in the rotation-affected regime, seen at $Pr = 0.1$ and $Ra/Ra_c \gtrsim 60$, u_{RMS} shows little variation with Ra/Ra_c, whereas the loss of rotational constraint (i.e. the decreasing importance of the Coriolis force) allows for larger vertical velocity fluctuations. In fact, their magnitude becomes as large as the horizontal fluctuations. This suggests that the flow approaches a rather isotropic dynamics, such as the one for non-rotating convection.

We have thus identified and discussed the characteristic force balance of the observed flow regimes of RRBC, as well as established connections between its changes with flow supercriticality and the transitions amongst these regimes. In particular, we have evaluated the r.m.s. value of the governing forces at midheight, and as such representative of the bulk. In the next section, we analyse the force balance close to the no-slip walls, and provide a comparison with the balance in the bulk.

4.3. *Force balance near no-slip walls*

In this section, we investigate the interplay between forces at a close distance from the no-slip walls. Specifically, we analyse the force balance at a distance δ_u from the bottom wall, where δ_u is the thickness of the kinetic boundary layer. Due to symmetry this analysis is also valid for the force balance near the top wall. The discrepancy between the force magnitudes computed at $z = \delta_u$ and those at $z = 1 - \delta_u$ (i.e. near the top wall) is less than 5 %. To determine the thickness δ_u of this layer, we adopt the conventional definition that uses the location of the peak value in the vertical profile of the r.m.s. horizontal velocity $u_{RMS}(z)$ (the profiles are time- and plane-averaged). We then employ (2.8) to determine the magnitudes of the forces at this height. The results are shown in figures 6(*a*), 6(*c*) and 6(*e*) for simulations at $Pr \approx 5$, 100 and 0.1, respectively. These figures show that also near the walls the flow is primarily geostrophic in regimes displaying cells, columns, plumes and

Flow	Dominant force balance	Subdominant force balance
Cells	$F_C \sim F_P$	$F_{ageos} \sim F_V$
Columns	$F_C \sim F_P$	$F_{ageos} \sim F_I \sim F_V$
Plumes	$F_C \sim F_P$	$F_{ageos} \sim F_I \sim F_V$
LSVs	$F_C \sim F_P$	$F_{ageos} \sim F_I$
RA convection	$F_I \sim F_P$	$F_C \sim F_V \sim F_B$

Table 3. Dominant and subdominant force balances at the kinetic boundary layer for each flow regime. As in table 2, $F_{ageos} = |\boldsymbol{F}_C + \boldsymbol{F}_P|$ measures the ageostrophy of the flow.

LSVs, whereas the rotational constraint is lost once it transitions to the rotation-affected regime. In particular, in figure 6(f), the transition from rotation-dominated ($Ro_\ell \lesssim 1$) to rotation-affected ($Ro_\ell \gtrsim 1$) convection occurs at approximately the same supercriticality as at midheight, i.e. $Ra/Ra_c \approx 60$ (at $Pr = 0.1$; compare figures 3f and 6f). Therefore, with increasing supercriticality, the flow loses rotational constraint at roughly equal Ra/Ra_c at both considered heights.

Figures 6(a) and 6(b) shows that, overall, the near-wall magnitude of the forces in the subdominant balance of cells, columns, plumes and LSVs is considerably larger than in the bulk. For instance, $|\boldsymbol{F}_C + \boldsymbol{F}_P| \sim 10^{-2}$ in the bulk and 10^{-1} near the walls (compare, e.g. the green symbols in figures 3a and 6a). This indicates that the flow is more ageostrophic near the walls. In the cellular and columnar regimes, such ageostrophy is largely caused by viscous forces (see figure 6a). The force balance per component, shown in figure 7, reveals that, in the presence of small vertical velocities w_{RMS} (due to Ekman pumping from the boundary layer; discussed below), the buoyancy force is closely balanced by the vertical pressure-gradient force (also in the plumes and LSV regime). Thus, cells and columns also exhibit a VAC balance close to the walls, in fair agreement with asymptotic simulations. Nonetheless, as in the bulk, the inertial force is seen to steeply increase with Ra/Ra_c, in fact, more sharply and dominantly near the walls than in the bulk (compare the grey stars in figures 3a and 6a). Consequently, F_I is part of the subdominant force balance in the columnar regime. The effects of inertia persist in the subdominant balance of plumes and LSVs. Therefore, in these two regimes, similar to the bulk, the near-wall flow adopts a CIA balance, with some participation of viscous forces. Eventually, F_I takes over the dominant force balance that, along with the reduction of the Coriolis force, leads to the transition to the rotation-affected regime. A summary of the dominant and subdominant force balances for all regimes is shown in table 3.

The early influence of inertial forces near the walls can be associated with the presence of large horizontal velocity fluctuations u_{RMS} at the site of convergence (divergence) of fluid due to Ekman pumping (suction), and the retardation of vertical velocities w_{RMS} near the walls. That is, considering the schematic in figure 8, the vertical flux wA_{cross} in a column/plume of cross-sectional area $A_{cross} = \pi R^2$ is fed by a boundary-layer flux uA_{cyl} through a cylindrical area $A_{cyl} = 2\pi R\delta_u$, where R is the typical radius of the columns/plumes. Hence, the fluxes must be equal, i.e. $wA_{cross} = uA_{cyl}$, from which we get $w/u = 2\delta_u/R$. From (2.6), $R \approx \ell_c/2 \sim Ek^{1/3}$. Furthermore, we expect $\delta_u \sim Ek^{1/2}$ for Ekman boundary layers (Pedlosky 1979). Therefore, $w/u \sim Ek^{1/6} \ll 1$. Thus, horizontal flow ($\sim u_{RMS}$) near the wall (inside the Ekman layer) is much larger than vertical flow ($\sim w_{RMS}$) emanating from the boundary layer. This is observed in figure 9. We note that also for stress-free cases (open symbols in figure 9), u_{RMS} is larger than w_{RMS}. In this case, a near-wall flux is also expected to feed the columns/plumes, though no estimation
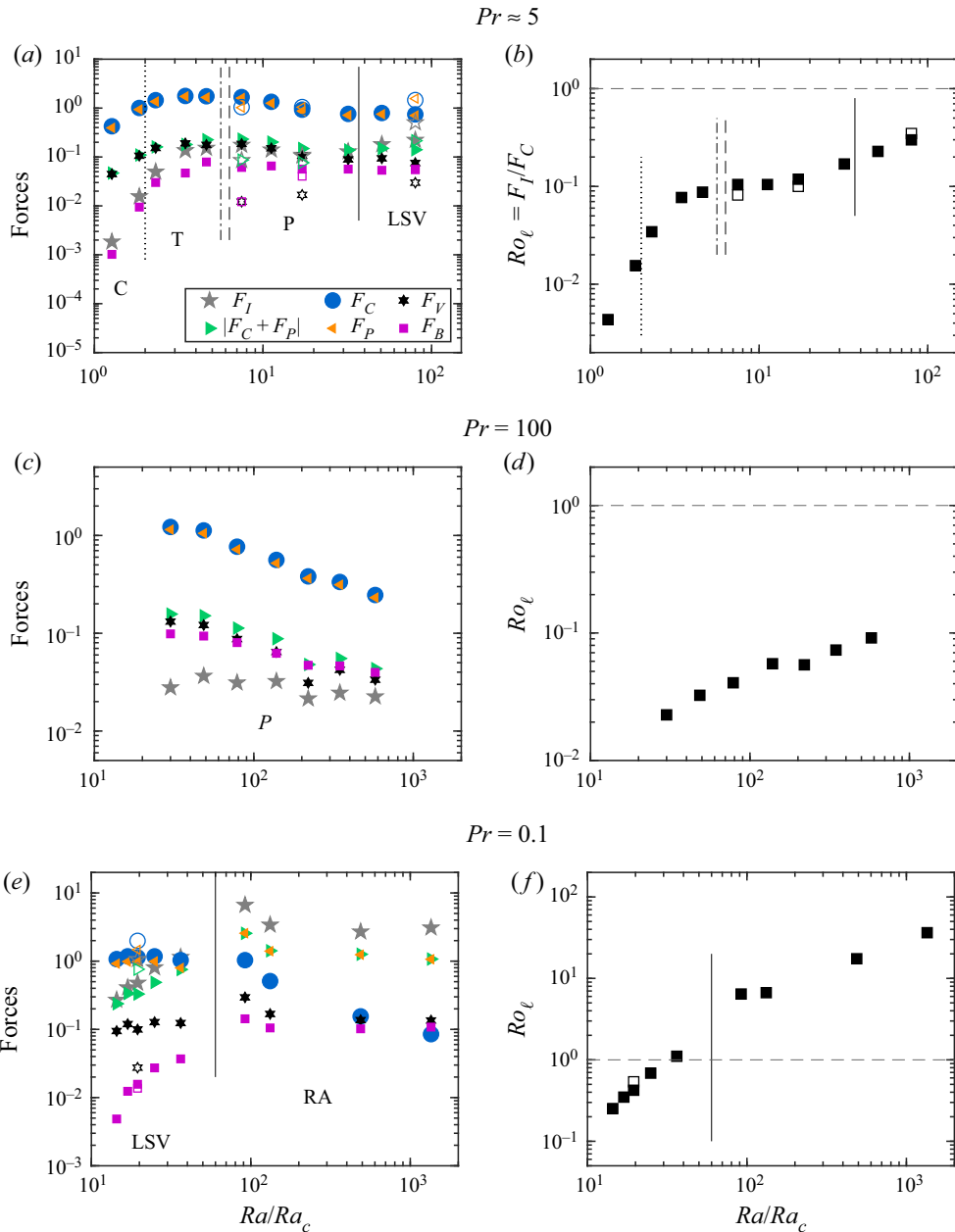
Figure 6. Force balance (*a,c,e*) and local Rossby number Ro_ℓ (*b,d,f*), both at the kinetic boundary layer, as a function of Ra/Ra_c for simulations at (*a,b*) $Pr \approx 5$, (*c,d*) 100 and (*e,f*) 0.1. Filled and open symbols correspond to simulations with no-slip and stress-free boundary conditions, respectively. Vertical and horizontal lines, as well as regime labels, are as in figure 3.

on its scaling can be currently made due to the scarcity of stress-free cases. Finally, the presence of inertial forces in the near-wall subdominant force balance does not necessarily imply the loss of vertical coherence as it does in the bulk (which causes the regime transition between columns and plumes). Yet, at larger Ra/Ra_c, the loss of rotational constraint close to the walls, which happens at roughly the same Ra/Ra_c as in the bulk,
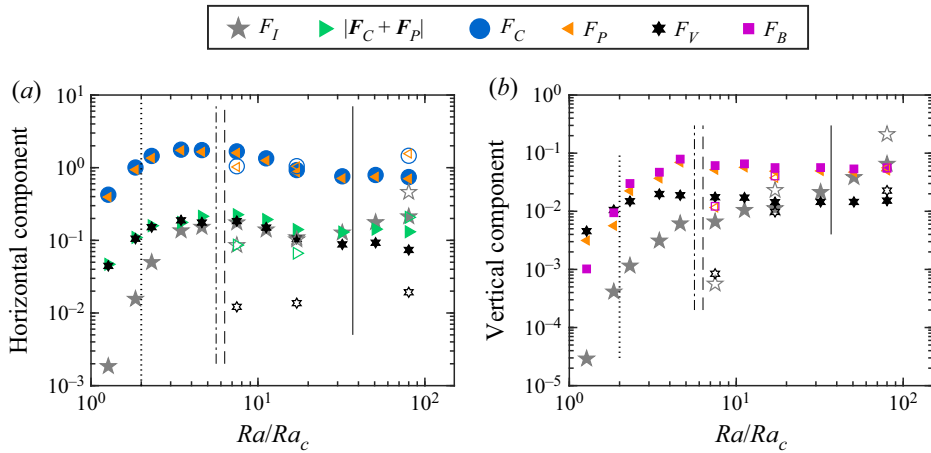
Figure 7. (*a*) Horizontal and (*b*) vertical force balance at the kinetic boundary layer as a function of the flow supercriticality Ra/Ra_c, for simulations at $Pr \approx 5$. Vertical lines are as in figure 3.
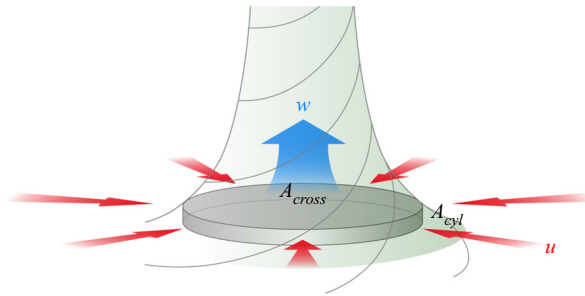

Figure 8. Schematic figure of geostrophic convection near a bottom no-slip wall. Vertical flux, wA_{cross}, in a column/plume of cross-sectional area, A_{cross}, is fed by a boundary-layer flux, uA_{cyl}, through a cylindrical area, A_{cyl}.

does suggest a nearly complete relaxation of the Taylor–Proudman constraint. This, along with the observed dominant role of inertial forces, has a great impact on the structure of the kinetic boundary layer. In a separate study, we find that the thickness δ_u of this layer scales as $Ek^{1/2}$ in all the geostrophic regimes (cells, columns, plumes and LSVs; at all Prandtl numbers), as predicted in linear Ekman boundary layer theory for rotationally constrained flows (Pedlosky 1979). However, in the rotation-affected regime (at $Pr = 0.1$), where the kinetic boundary layer is no longer rotationally constrained, δ_u does not exhibit the theoretical scaling $Ek^{1/2}$. Therefore, the kinetic boundary layer at values of Ra/Ra_c beyond the geostrophically balanced regimes is certainly not of Ekman type. The loss of rotational constraint in the near-wall region may allude to a transition to the proposed 'unbalanced boundary layer' regime for $Ek \lesssim 10^{-7}$ (Cheng *et al.* 2018), distinguished by the breakdown of geostrophy in the thermal boundary layers. In this regime, nonetheless, the flow is not well-understood and warrants further investigation.

5. Conclusions

To summarise, we find that in rapidly rotating Rayleigh–Bénard convection the dominant force balance is geostrophy, the balance between the Coriolis force and the
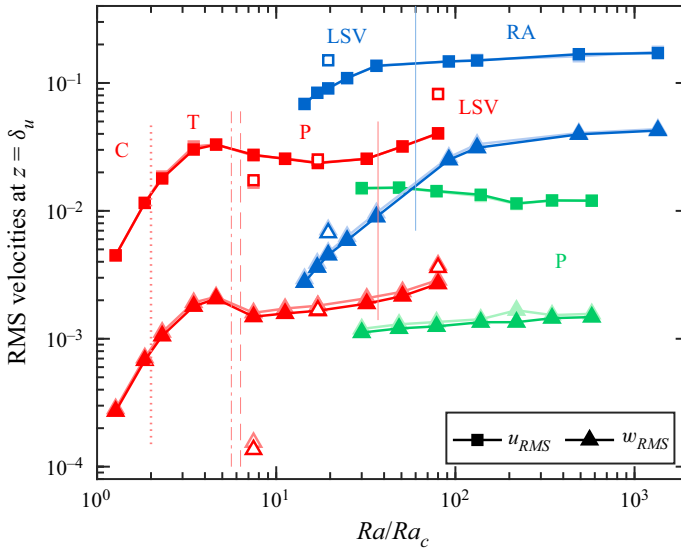
Figure 9. Root mean square of horizontal and vertical velocities, u_{RMS} and w_{RMS}, at the bottom kinetic boundary layer ($z = \delta_u$, dark-coloured symbols) and at the top kinetic boundary layer ($z = 1 - \delta_u$, light-coloured symbols). Filled and open symbols correspond to simulations with no-slip and stress-free boundary conditions, respectively. Red, green and blue symbols are results from simulations at $Pr \approx 5$, 100 and 0.1, respectively. Colour-coded vertical lines are as in figure 3.

pressure-gradient force, as anticipated in previous literature (Sprague *et al.* 2006; Julien *et al.* 2012; Nieves *et al.* 2014; Plumley *et al.* 2016). The geostrophic regimes display cells, convective Taylor columns, plumes and large-scale vortices. We find that in these regimes the flow is also in leading geostrophic balance near the no-slip walls.

In simulations at $Pr = 0.1$, we find that the geostrophic balance breaks down at large supercriticality past the regime of large-scale vortices. This results in the flow transition from the rotation-dominated state to rotation-affected convection. This transition originates from the sudden decrease of the magnitude of the Coriolis force, along with an increment in the strength of inertial forces. We find that this loss of rotational constraint occurs synchronously (at approximately the same Ra/Ra_c) in the bulk and in the boundary-layer region.

The geostrophic flows are ageostrophic at higher order, caused by the contribution of the remaining forces (inertia, viscous and buoyancy forces). For cells and columns, ageostrophy is due to viscosity and buoyancy, thus leading to a VAC balance. Inertia is smaller, but steeply increases with Ra/Ra_c. For plumes, inertial forces enter the subdominant balance, along with viscous and buoyancy forces. For LSVs, inertia becomes the main source of ageostrophy. Plumes and LSVs can be considered in CIA balance, with some participation of viscous forces in the plumes regime. In rotation-affected convection, inertial and pressure-gradient forces constitute the dominant force balance; the subdominant balance is formed by the Coriolis, viscous and buoyancy forces.

In the bulk, the presence of inertial forces in the subdominant force balance marks the loss of vertical coherence of the columnar structures in the flow, and thus the commencement of the plumes regime. Near the no-slip boundaries, inertial effects become part of the subdominant force balance at smaller Ra/Ra_c within the columnar regime, although, remarkably, without deteriorating their structure. The reason is that, near the walls, this enhanced inertial force results from the convergence (and divergence) of fluid

to the site of formation of vortical structures at the Ekman boundary layer. This effect persists in the subdominant force balance of plumes and LSVs.

Whilst buoyancy displays a leading participation in the vertical force balance near the walls, its role may be negligible in the overall dominant (or even subdominant) force balance for cells, columns and plumes. This is in contrast to the bulk, where the buoyancy force participates in the subdominant balance. This is despite having approximately the same order of magnitude ($\sim 10^{-2}$) at both locations. The reason is that viscous forces (for cells, columns and plumes) and inertial forces (for columns and plumes) are approximately one order of magnitude larger close to the boundaries, thus increasing the overall degree of ageostrophy of the flow by one order of magnitude in this region.

Declaration of interests. The authors report no conflict of interest.

Data availability statement. The data that support the findings of this study are available from the corresponding author, R.P.J.K., upon reasonable request.

Author ORCIDs.

Andrés J. Aguirre Guzmán https://orcid.org/0000-0002-4942-5216;

Matteo Madonia https://orcid.org/0000-0002-8510-8103;

Jonathan S. Cheng https://orcid.org/0000-0002-2326-9614;

Rodolfo Ostilla-Mónico https://orcid.org/0000-0001-7049-2432;

Herman J.H. Clercx https://orcid.org/0000-0001-8769-0435;

Rudie P.J. Kunnen https://orcid.org/0000-0002-1219-694X.

Author contributions. A.J.A.G. performed the simulations, analysed the data and drafted the manuscript. M.M., J.S.C. and R.O.M. aided in interpreting the results. H.J.H.C. and R.P.J.K. designed the study and supervised the work. All authors provided critical feedback on the final version of the manuscript.

REFERENCES

AGUIRRE GUZMÁN, A.J., MADONIA, M., CHENG, J.S., OSTILLA-MÓNICO, R., CLERCX, H.J.H. & KUNNEN, R.P.J. 2020 Competition between Ekman plumes and vortex condensates in rapidly rotating thermal convection. *Phys. Rev. Lett.* **125** (21), 214501.

AHLERS, G., GROSSMANN, S. & LOHSE, D. 2009 Heat transfer and large scale dynamics in turbulent Rayleigh–Bénard convection. *Rev. Mod. Phys.* **81** (2), 503.

AUBERT, J. 2005 Steady zonal flows in spherical shell dynamos. *J. Fluid Mech.* **542**, 53–67.

AUBERT, J. 2019 Approaching Earth's core conditions in high-resolution geodynamo simulations. *Geophys. J. Intl* **219** (Supplement_1), S137–S151.

AUBERT, J., BRITO, D., NATAF, H.C., CARDIN, P. & MASSON, J.P. 2001 A systematic experimental study of rapidly rotating spherical convection in water and liquid gallium. *Phys. Earth Planet. Inter.* **128** (1–4), 51–74.

AUBERT, J., GASTINE, T. & FOURNIER, A. 2017 Spherical convective dynamos in the rapidly rotating asymptotic regime. *J. Fluid Mech.* **813**, 558–593.

AUBERT, J., GILLET, N. & CARDIN, P. 2003 Quasigeostrophic models of convection in rotating spherical shells. *Geochem. Geophys.* **4** (7), 1052.

AURNOU, J.M., BERTIN, V., GRANNAN, A.M., HORN, S. & VOGT, T. 2018 Rotating thermal convection in liquid gallium: multi-modal flow, absent steady columns. *J. Fluid Mech.* **846**, 846–876.

AURNOU, J.M., CALKINS, M.A., CHENG, J.S., JULIEN, K., KING, E.M., NIEVES, D., SODERLUND, K.M. & STELLMACH, S. 2015 Rotating convective turbulence in Earth and planetary cores. *Phys. Earth Planet. Inter.* **246**, 52–71.

AURNOU, J.M., HORN, S. & JULIEN, K. 2020 Connections between nonrotating, slowly rotating, and rapidly rotating turbulent convection transport scalings. *Phys. Rev. Res.* **2** (4), 043115.

BALBUS, S.A., BONART, J., LATTER, H.N. & WEISS, N.O. 2009 Differential rotation and convection in the Sun. *Mon. Not. R. Astron. Soc.* **400** (1), 176–182.

BUDÉUS, G., CISEWSKI, B., RONSKI, S., DIETRICH, D. & WEITERE, M. 2004 Structure and effects of a long lived vortex in the Greenland Sea. *Geophys. Res. Lett.* **31** (5), L05304.

BUSSE, F.H. 1970 Thermal instabilities in rapidly rotating systems. *J. Fluid Mech.* **44** (3), 441–460.

BUSSE, F.H. 1994 Convection driven zonal flows and vortices in the major planets. *Chaos* **4** (2), 123–134.

BUSSE, F.H. & CARRIGAN, C.R. 1976 Laboratory simulation of thermal convection in rotating planets and stars. *Science* **191** (4222), 81–83.

CABANES, S., AURNOU, J., FAVIER, B. & LE BARS, M. 2017 A laboratory model for deep-seated jets on the gas giants. *Nat. Phys.* **13** (4), 387–390.

CALKINS, M.A., JULIEN, K., TOBIAS, S.M. & AURNOU, J.M. 2015 A multiscale dynamo model driven by quasi-geostrophic convection. *J. Fluid Mech.* **780**, 143–166.

CALKINS, M.A., NOIR, J., ELDREDGE, J.D. & AURNOU, J.M. 2012 The effects of boundary topography on convection in Earth's core. *Geophys. J. Intl* **189** (2), 799–814.

CARDIN, P. & OLSON, P. 1994 Chaotic thermal convection in a rapidly rotating spherical shell: consequences for flow in the outer core. *Phys. Earth Planet. Inter.* **82** (3–4), 235–259.

CASTAING, B., GUNARATNE, G., HESLOT, F., KADANOFF, L., LIBCHABER, A., THOMAE, S., WU, X.-Z., ZALESKI, S. & ZANETTI, G. 1989 Scaling of hard thermal turbulence in Rayleigh–Bénard convection. *J. Fluid Mech.* **204**, 1–30.

CATTANEO, F., EMONET, T. & WEISS, N. 2003 On the interaction between convection and magnetic fields. *Astrophys. J.* **588** (2), 1183.

CHANDRASEKHAR, S. 1961 *Hydrodynamic and Hydromagnetic Stability*. Oxford University Press.

CHARNEY, J.G. 1948 On the scale of atmospheric motions. In *Geophys. Publ.*, pp. 3–17.

CHARNEY, J.G. 1971 Geostrophic turbulence. *J. Atmos. Sci.* **28** (6), 1087–1095.

CHENG, J.S., AURNOU, J.M., JULIEN, K. & KUNNEN, R.P.J. 2018 A heuristic framework for next-generation models of geostrophic convective turbulence. *Geophys. Astrophys. Fluid Dyn.* **112** (4), 277–300.

CHENG, J.S., MADONIA, M., AGUIRRE GUZMÁN, A.J. & KUNNEN, R.P.J. 2020 Laboratory exploration of heat transfer regimes in rapidly rotating turbulent convection. *Phys. Rev. Fluids* **5** (11), 113501.

CHENG, J.S., STELLMACH, S., RIBEIRO, A., GRANNAN, A., KING, E.M. & AURNOU, J.M. 2015 Laboratory-numerical models of rapidly rotating convection in planetary cores. *Geophys. J. Intl* **201** (1), 1–17.

CHONG, K.L., SHI, J.-Q., DING, G.-Y., DING, S.-S., LU, H.-Y., ZHONG, J.-Q. & XIA, K.-Q. 2020 Vortices as Brownian particles in turbulent flows. *Sci. Adv.* **6** (34), eaaz1110.

CHRISTENSEN, U.R. 2002 Zonal flow driven by strongly supercritical convection in rotating spherical shells. *J. Fluid Mech.* **470**, 115–133.

ECKE, R.E. & NIEMELA, J.J. 2014 Heat transport in the geostrophic regime of rotating Rayleigh–Bénard convection. *Phys. Rev. Lett.* **113** (11), 114301.

GASCARD, J.-C., WATSON, A.J., MESSIAS, M.-J., OLSSON, K.A., JOHANNESSEN, T. & SIMONSEN, K. 2002 Long-lived vortices as a mode of deep ventilation in the Greenland Sea. *Nature* **416** (6880), 525–527.

GASTINE, T., WICHT, J. & AUBERT, J. 2016 Scaling regimes in spherical shell rotating convection. *J. Fluid Mech.* **808**, 690–732.

GILLET, N. & JONES, C.A. 2006 The quasi-geostrophic model for rapidly rotating spherical convection outside the tangent cylinder. *J. Fluid Mech.* **554**, 343–369.

GLATZMAIER, G.A., COE, R.S., HONGRE, L. & ROBERTS, P.H. 1999 The role of the Earth's mantle in controlling the frequency of geomagnetic reversals. *Nature* **401** (6756), 885–890.

GROOMS, I., JULIEN, K., WEISS, J.B. & KNOBLOCH, E. 2010 Model of convective Taylor columns in rotating Rayleigh–Bénard convection. *Phys. Rev. Lett.* **104** (22), 224501.

GUERVILLY, C., CARDIN, P. & SCHAEFFER, N. 2019 Turbulent convective length scale in planetary cores. *Nature* **570** (7761), 368–371.

HADLEY, G. 1735 Concerning the cause of the general trade-winds. *Phil. Trans. R. Soc. Lond.* **39** (437), 58–62.

HEARD, W.B. & VERONIS, G. 1971 Asymptotic treatment of the stability of a rotating layer of fluid with rigid boundaries. *Geophys. Fluid Dyn.* **2** (1), 299–316.

HEIMPEL, M. & AURNOU, J.M. 2007 Turbulent convection in rapidly rotating spherical shells: a model for equatorial and high latitude jets on Jupiter and Saturn. *Icarus* **187** (2), 540–557.

HEIMPEL, M., GASTINE, T. & WICHT, J. 2016 Simulation of deep-seated zonal jets and shallow vortices in gas giant atmospheres. *Nat. Geosci.* **9** (1), 19–23.

HINDMAN, B.W., FEATHERSTONE, N.A. & JULIEN, K. 2020 Morphological classification of the convective regimes in rotating stars. *Astrophys. J.* **898** (2), 120.

INGERSOLL, A.P. 1990 Atmospheric dynamics of the outer planets. *Science* **248** (4953), 308–315.

JONES, C.A. 2000 Convection–driven geodynamo models. *Phil. Trans. R. Soc. Lond.* A **358** (1768), 873–897.

JULIEN, K., AURNOU, J.M., CALKINS, M.A., KNOBLOCH, E., MARTI, P., STELLMACH, S. & VASIL, G.M. 2016 A nonlinear model for rotationally constrained convection with Ekman pumping. *J. Fluid Mech.* **798**, 50–87.

JULIEN, K., KNOBLOCH, E., MILLIFF, R. & WERNE, J. 2006 Generalized quasi-geostrophy for spatially anisotropic rotationally constrained flows. *J. Fluid Mech.* **555**, 233–274.

JULIEN, K., KNOBLOCH, E. & WERNE, J. 1998 A new class of equations for rotationally constrained flows. *Theor. Comput. Fluid Dyn.* **11** (3), 251–261.

JULIEN, K., RUBIO, A.M., GROOMS, I. & KNOBLOCH, E. 2012 Statistical and physical balances in low Rossby number Rayleigh–Bénard convection. *Geophys. Astrophys. Fluid Dyn.* **106** (4–5), 392–428.

KERR, R.M. 1996 Rayleigh number scaling in numerical convection. *J. Fluid Mech.* **310**, 139–179.

KING, E.M. & AURNOU, J.M. 2012 Thermal evidence for Taylor columns in turbulent rotating Rayleigh–Bénard convection. *Phys. Rev.* E **85** (1), 016313.

KING, E.M. & BUFFETT, B.A. 2013 Flow speeds and length scales in geodynamo models: the role of viscosity. *Earth Planet. Sci. Lett.* **371**, 156–162.

KING, E.M., STELLMACH, S. & BUFFETT, B. 2013 Scaling behaviour in Rayleigh–Bénard convection with and without rotation. *J. Fluid Mech.* **717**, 449–471.

KRAICHNAN, R.H. 1962 Turbulent thermal convection at arbitrary Prandtl number. *Phys. Fluids* **5** (11), 1374–1389.

KUNNEN, R.P.J. 2021 The geostrophic regime of rapidly rotating turbulent convection. *J. Turbul.* **22** (4–5), 267–296.

KUNNEN, R.P.J., CLERCX, H.J.H. & GEURTS, B.J. 2010 Vortex statistics in turbulent rotating convection. *Phys. Rev.* E **82** (3), 036306.

KUNNEN, R.P.J., GEURTS, B.J. & CLERCX, H.J.H. 2009 Turbulence statistics and energy budget in rotating Rayleigh–Bénard convection. *Eur. J. Mech.* B*/Fluids* **28** (4), 578–589.

KUNNEN, R.P.J., OSTILLA-MÓNICO, R., VAN DER POEL, E.P., VERZICCO, R. & LOHSE, D. 2016 Transition to geostrophic convection: the role of the boundary conditions. *J. Fluid Mech.* **799**, 413–432.

LOHSE, D. & XIA, K.-Q. 2010 Small-scale properties of turbulent Rayleigh–Bénard convection. *Annu. Rev. Fluid Mech.* **42**, 335–364.

MAFFEI, S., KROUSS, M.J., JULIEN, K. & CALKINS, M.A. 2021 On the inverse cascade and flow speed scaling behaviour in rapidly rotating Rayleigh–Bénard convection. *J. Fluid Mech.* **913**, A18.

MALKUS, W.V.R. 1954 The heat transport and spectrum of thermal turbulence. *Proc. R. Soc. Lond.* A **225** (1161), 196–212.

MARSHALL, J. & SCHOTT, F. 1999 Open-ocean convection: observations, theory, and models. *Rev. Geophys.* **37** (1), 1–64.

MIESCH, M.S. 2000 The coupling of solar convection and rotation. *Solar Phys.* **192**, 59–89.

NIEVES, D., RUBIO, A.M. & JULIEN, K. 2014 Statistical classification of flow morphology in rapidly rotating Rayleigh–Bénard convection. *Phys. Fluids* **26** (8), 086602.

NOTO, D., TASAKA, Y., YANAGISAWA, T. & MURAI, Y. 2019 Horizontal diffusive motion of columnar vortices in rotating Rayleigh–Benard convection. *J. Fluid Mech.* **871**, 401–426.

OSTILLA-MÓNICO, R., YANG, Y., VAN DER POEL, E.P., LOHSE, D. & VERZICCO, R. 2015 A multi-resolution strategy for direct numerical simulation of scalar turbulence. *J. Comput. Phys.* **301**, 308–321.

PEDLOSKY, J. 1979 *Geophysical Fluid Dynamics*. Springer.

PLUMLEY, M., JULIEN, K., MARTI, P. & STELLMACH, S. 2016 The effects of Ekman pumping on quasi-geostrophic Rayleigh–Bénard convection. *J. Fluid Mech.* **803**, 51–71.

PORCO, C.C., *et al.* 2003 Cassini imaging of Jupiter's atmosphere, satellites, and rings. *Science* **299** (5612), 1541–1547.

PORTEGIES, J.W., KUNNEN, R.P.J., VAN HEIJST, G.J.F. & MOLENAAR, J. 2008 A model for vortical plumes in rotating convection. *Phys. Fluids* **20**, 066602.

PROUDMAN, J. 1916 On the motion of solids in a liquid possessing vorticity. *Proc. R. Soc. Lond.* A **92** (642), 408–424.

RAJAEI, H., KUNNEN, R.P.J. & CLERCX, H.J.H. 2017 Exploring the geostrophic regime of rapidly rotating convection with experiments. *Phys. Fluids* **29** (4), 045105.

RUBIO, A.M., JULIEN, K., KNOBLOCH, E. & WEISS, J.B. 2014 Upscale energy transfer in three-dimensional rapidly rotating turbulent convection. *Phys. Rev. Lett.* **112** (14), 144501.

SAKAI, S. 1997 The horizontal scale of rotating convection in the geostrophic regime. *J. Fluid Mech.* **333**, 85–95.

SANCHEZ-LAVEGA, A., ROJAS, J.F. & SADA, P.V. 2000 Saturn's zonal winds at cloud level. *Icarus* **147** (2), 405–420.

SARSON, G.R. 2000 Reversal models from dynamo calculations. *Phil. Trans. R. Soc. Lond.* A **358** (1768), 921–942.

SCHAEFFER, N., JAULT, D., NATAF, H.-C. & FOURNIER, A. 2017 Turbulent geodynamo simulations: a leap towards Earth's core. *Geophys. J. Intl* **211** (1), 1–29.

SCHWAIGER, T., GASTINE, T. & AUBERT, J. 2019 Force balance in numerical geodynamo simulations: a systematic study. *Geophys. J. Intl* **219** (Supplement_1), S101–S114.

SCHWAIGER, T., GASTINE, T. & AUBERT, J. 2021 Relating force balances and flow length scales in geodynamo simulations. *Geophys. J. Intl* **224** (3), 1890–1904.

SHI, J.-Q., LU, H.-Y., DING, S.-S. & ZHONG, J.-Q. 2020 Fine vortex structure and flow transition to the geostrophic regime in rotating Rayleigh–Bénardnard convection. *Phys. Rev. Fluids* **5** (1), 011501.

SHRAIMAN, B.I. & SIGGIA, E.D. 1990 Heat transport in high-Rayleigh-number convection. *Phys. Rev.* A **42** (6), 3650.

SODERLUND, K.M., KING, E.M. & AURNOU, J.M. 2012 The influence of magnetic fields in planetary dynamo models. *Earth Planet. Sci. Lett.* **333**, 9–20.

SPIEGEL, E.A. 1971 Convection in stars I. Basic Boussinesq convection. *Annu. Rev. Astron. Astrophys.* **9** (1), 323–352.

SPRAGUE, M., JULIEN, K., KNOBLOCH, E. & WERNE, J. 2006 Numerical simulation of an asymptotically reduced system for rotationally constrained convection. *J. Fluid Mech.* **551**, 141–174.

STELLMACH, S., LISCHPER, M., JULIEN, K., VASIL, G., CHENG, J.S., RIBEIRO, A., KING, E.M. & AURNOU, J.M. 2014 Approaching the asymptotic regime of rapidly rotating convection: boundary layers versus interior dynamics. *Phys. Rev. Lett.* **113** (25), 254501.

STEVENSON, D.J. 1979 Turbulent thermal convection in the presence of rotation and a magnetic field: a heuristic theory. *Geophys. Astrophys. Fluid Dyn.* **12** (1), 139–169.

TAYLOR, G.I. 1917 Motion of solids in fluids when the flow is not irrotational. *Proc. R. Soc. Lond.* A **93** (648), 99–113.

VERZICCO, R. & CAMUSSI, R. 2003 Numerical experiments on strongly turbulent thermal convection in a slender cylindrical cell. *J. Fluid Mech.* **477**, 19–49.

VERZICCO, R. & ORLANDI, P. 1996 A finite-difference scheme for three-dimensional incompressible flows in cylindrical coordinates. *J. Comput. Phys.* **123** (2), 402–414.

WADHAMS, P., HOLFORT, J., HANSEN, E. & WILKINSON, J.P. 2002 A deep convective chimney in the winter Greenland Sea. *Geophys. Res. Lett.* **29** (10), 1434.

YADAV, R.K. & BLOXHAM, J. 2020 Deep rotating convection generates the polar hexagon on Saturn. *Proc. Natl Acad. Sci.* **117** (25), 13991–13996.

YADAV, R.K., GASTINE, T., CHRISTENSEN, U.R., WOLK, S.J. & POPPENHAEGER, K. 2016 Approaching a realistic force balance in geodynamo simulations. *Proc. Natl Acad. Sci.* **113** (43), 12065–12070.